

Microstructures and Properties of Cold Spray Nanostructured HA Coatings

Xiao Chen^{1,2} · Gangchang Ji² · Xiaobo Bai² · Hailong Yao² · Qingyu Chen² · Yanlong Zou²

Submitted: 7 June 2018 / in revised form: 11 August 2018 / Published online: 25 October 2018
© ASM International 2018

Abstract Nanostructured hydroxyapatite (nHA) coatings on implant surface are highly desirable owing to their excellent osteoconductive properties in association with intrinsic small crystals. Low processing temperature of cold spray makes it an ideal technique to prepare nHA coatings with nanostructured feedstock. This work demonstrated that dense and thick nHA coatings were achievable by cold spraying nanostructured feedstock onto TC4 alloy surface. Coating formation mechanisms were explored by investigating the deposition of individual particles. Microstructures, mechanical profiles and biological properties of the coatings were comprehensively investigated. A porous Ti buffer layer significantly enhanced the bonding between nHA coatings and the substrate. As-deposited nHA coatings exhibited a high wear resistance when slid against polyurethane or polycarbonate and a strong apatite-forming ability when being immersed in simulated body fluid (SBF). Findings of this work will contribute to a comprehensive understanding of building mechanisms, structures and properties of cold sprayed nHA coatings.

Keywords biological properties · cold spray · mechanical properties · microstructure · nanohydroxyapatite

Xiao Chen and Gangchang Ji have contributed equally to this work.

✉ Gangchang Ji
j8g3c1@126.com

¹ School of Mechanical and Electrical Engineering, XinYu University, Xinyu 338004, China

² Jiangxi Province Engineering Research Center of Materials Surface Enhancing and Remanufacturing, School of Mechanical and Materials Engineering, Jiujiang University, Jiujiang 332005, Jiangxi, China

Introduction

Hydroxyapatite is an applicable biocompatible and bioactive coating material used in load-bearing implants due to its ideal biological properties and comparable mechanical properties with bones (Ref 1). To date, a variety of processes have been developed to deposit HA coatings, including electrochemical deposition (Ref 2), seeded hydrothermal deposition (Ref 3) electrophoretic deposition (Ref 4), electrodeposition (Ref 5), sol–gel (Ref 6), micro-arc oxidation (Ref 7), sputtering (Ref 8), sintering (Ref 9), friction stir processing (Ref 10), dip coating (Ref 11), pulsed laser deposition (Ref 12), plasma spray (PS) (Ref 1, 13), microplasma spray (Ref 14), high-velocity oxygen fuel spray (Ref 15), and suspension spray (Ref 16). Among these processes, PS is most commonly used as an industrial way to coat HA on Ti implant due to its relatively high depositing efficiency and high coating hardness (Ref 16). Nevertheless, some issues for PS deposited HA coatings such as the decomposition of feedstock particles and formation of amorphous phase can be problematic (Ref 17).

Many efforts have been dedicated to elucidate the structural evolution of thermal sprayed HA-based coatings during coating deposition (Ref 15, 17). Thermally induced decomposition and/or phase transformation of HA particles has been reported to lead to the formation of tricalcium phosphate (TCP), tetracalcium phosphate (TTCP) and CaO phases (Ref 15, 18). In addition, rapid quenching of fully molten HA particles onto the ambient temperature substrate can cause the generation of amorphous phase (ACP) and low crystallinity of resultant coatings (Ref 15, 18). Therefore, it is inferred that decreasing the processing temperature can potentially suppress the decomposition of HA and formation of undesirable phases.

The low processing temperature of cold spray makes it an ideal technique to prepare HA coatings. During cold spray process, feedstock particles are accelerated to supersonic velocities by a supersonic gas jet and then impact onto the substrate surface. The bonding of deposited particles to the substrate mainly derives from high-velocity impact induced severe plastic deformation of the particles and/or substrate at a completely solid state (Ref 19).

To date, cold spray process has been successfully employed to deposit a wide range of plastically deformable metallic coatings such as Al (Ref 20), Cu (Ref 21), Ti (Ref 22), Fe (Ref 21) and Ni-Cr (Ref 23). Owing to its low processing temperature, cold spray was also applied to deposit thermal sensitive materials (Ref 24) and biomaterial coatings (Ref 25) as well as WC-Co coatings to maintain the original structures of the feedstock materials (Ref 26). Recently, some investigators explored the pathway to deposit HA and its composite coatings by using cold spraying (CS) technique and identified the feasibility to fabricate HA coatings (Ref 27). These pioneering studies paved a new pathway to build HA coatings. As the nanostructured HA exhibits an enhanced bioactivity in comparison with conventional HA (Ref 2), nevertheless, formation mechanisms of cold sprayed nHA coatings are not fully understood yet. It is thus of fundamental importance to investigate the deformation behavior of cold sprayed nHA splats and the structure–property relationship of nHA coatings. In the present work, building mechanisms, structures and properties, i.e., bonding strength, abrasion resistance and biological compatibility, of cold sprayed nHA coatings were comprehensively investigated to gain insight into the structure–property relationship of the nHA coatings.

Materials and Experimental Procedures

In this study, nHA coatings were deposited onto a TC4 alloy substrate by cold spray. Due to the huge hardness mismatch between TC4 substrate and nHA particle, it is difficult to directly deposit nHA onto the substrate. Hence, a 60 μm thick Ti coating was cold sprayed onto the TC4 substrate as a buffer layer. It was also expected to get strong adhesive strength of the nHA coating due to the high surface roughness of the cold sprayed Ti buffer layer. Microstructure and composition of individual splats and the coatings were characterized. Mechanical properties of the coatings in terms of microhardness, adhesion strength and wear resistance were examined.

Materials

Pure Ti powders with an irregular morphology (Beijing Dk Nano technology Co., LTD, Beijing, China) were used as the feedstock to deposit the buffer layer. Commercially

available flocculent nanohydroxyapatite (nHA) powders (Beijing Dk Nano technology Co., LTD, Beijing, China) were used as the feedstock to deposit nHA coatings.

Commercial TC4 alloy (Ti6Al4V) used as the substrate had a size of 15 mm \times 50 mm \times 5 mm. Cylindrical specimens were used for biological properties, abrasive wear and tensile strength measurements, with dimensions of Φ 6 mm \times 15 mm and Φ 25.4 mm \times 50 mm, respectively. The substrates were grit blasted with 24 mesh alumina grits prior to coating deposition and then sonicated in an acetone bath. Substrates for depositing single particles were ground and polished to a mirror finish and finally sonicated in an acetone bath.

Commercially available Hanks' balanced salt solution (H1025, Solarbio material co., Beijing, China) was used as the SBF (composition, NaCl: 8 g/L, $\text{Na}_2\text{HPO}_4 \cdot 12\text{H}_2\text{O}$: 0.126 g/L, KCl: 0.4 g/L, KH_2PO_4 : 0.06 g/L, MgSO_4 : 0.098 g/L, CaCl_2 : 0.14 g/L, D-glucose: 1 g/L, and NaHCO_3 : 0.35 g/L).

Coating Deposition

A CS-2000 model cold spraying system (CS-2000 model, developed by Xi'an Jiaotong University, Shanxi, China) was used to deposit both the Ti buffer layer and nHA coatings. A schematic diagram of the spraying system is shown in Fig. 1. Detailed information about this system was available elsewhere (Ref 26). A Ti buffer layer with a thickness of about 60 μm was deposited onto TC4 substrate. nHA coatings were deposited above the buffer layer with a thickness of about 120 μm . Nitrogen gas was used as the carrier and accelerating gas. Detailed spray parameters are listed in Table 1.

Powder and Coating Microstructure Characterization

Morphologies of the powders were characterization by using scanning electron microscopy (SEM, VEGA II-LSU, TESCAN, Czech). Size distributions of the both kinds of powders were measured by a laser diffraction meter (Malvern Mastersizer 2000, Malvern instrument Ltd. UK).

Phase constitutions of both original powders and as-sprayed coatings were analyzed by XRD using a Bruker D8 Advance diffract-meter with a copper radiation source ($\text{CuK}\alpha$, $\lambda = 1.5418 \text{ \AA}$) operated at 35 kV and 35 mA. The crystallinity of nHA coatings was calculated by the following equation (Ref 28):

$$\text{Crystallinity}(\%) = \frac{\sum A_c}{\left(\sum A_c + \sum A_a\right)} \times 100\% \quad (\text{Eq 1})$$

where $\sum A_c$ and $\sum A_a$ were, respectively, the total area under crystal HA peaks and total area of amorphous phase under all peaks in XRD patterns.

Fig. 1 A schematic diagram showing the working principle of the cold spray system: 1. console cabinet; 2. valve; 3. gas heater; 4. accelerating gas pipe; 5. spray gun; 6. powder feeder; 7. thermal couples; 8. display panel; 9. carrier gas; 10. powder feeder gas inlet; 11. accelerating gas inlet

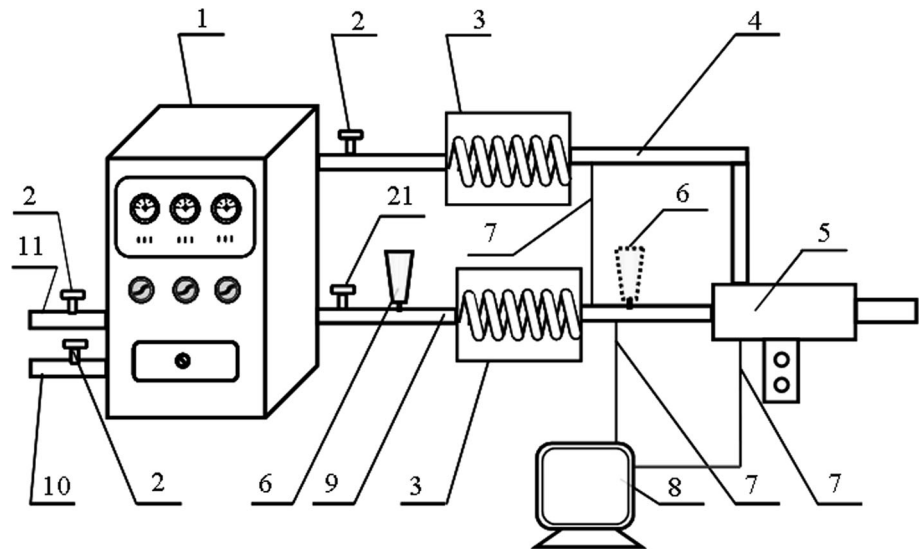


Table 1 The parameters of cold spraying

	Ti particle	Ti coating	nHA particle	Ti coating
Working gas pressure, MPa	2.0	2.0	2.0	2.0
Powder feed gas pressure, MPa	2.2	2.2	2.2	2.2
Gas temperature in gun chamber, °C	300 ± 10	300 ± 30	300 ± 10	300 ± 30
Spray distance, mm	10	10	10	10
Transverse speed of gun, mm s ⁻¹	500	150	300	30

Cross-sectional microstructures of nHA coatings, surface morphologies of the original powders, Ti buffer layer and nHA coatings in both as-sprayed and after SBF immersion were examined via the SEM (VEGA II-LSU, TESCAN, Czech). Structures of original nHA powders and as-sprayed nHA coatings were analyzed by Fourier Transform Infrared Spectroscopy (FTIR, MX-1E, Nicolet, VERTEX 70, Bruker Germany).

The porosity of nHA coating was determined by nitrogen adsorption–desorption isotherms at 77 K (TriStarII3020, Micromeritics Instrument Corporation, USA). The pore size distribution (pore diameter and pore volume) were evaluated from the desorption branches of isotherms based on Barrett-Joyner-Halenda (BJH) method.

Microhardness, Adhesion Strength and Abrasive Wear Test

Vickers microhardness indents were made on the polished coating cross section by a Shimadzu Type M Vickers indenter Tester (HVS-1000, Shanghai, China). The final hardness value was taken as an average of 15 indentations performed on each sample. The applied load and dwelling time for measuring were 10 gf and 15 s, respectively.

Adhesion strength of as-sprayed nHA coatings was measured using standard tensile test (ASTM C633). The

end surface of cylindrical samples with deposited coatings was bonded to grit-blasted facings of the loading fixtures, with the same size of the sample, using special adhesive glue (E-7, Adtest, Shanghai Huayi Resins Co. Ltd., China) with an intrinsic strength of about 70 MPa. The assembly was then held perpendicularly in an oven at 100 °C for 2 h. After the adhesive cured, the assembly was loaded in the tensile tester (ZWICK, Z050 model) at an extension speed of 1 mm/min. The bond strength of nHA coating was evaluated by the average value of three testing results.

Wear tests were carried out under dry sliding conditions using a pin-on-disk tester (Model ML-100, Zhangjiakou Chengxin Balance Testing Machineries Company, China). In order to characterize the wear behaviors of nHA coatings slid against counterparts similar to the artificial ligament material, polycarbonate (PC) and polyurethane (PU) sheets with thickness of about 1 mm were adhered to the disk surface, respectively. During the tests, the coating surface was loaded against a rotating disk with a contact load of 2 N. The rotation speed of disk, radial feed rate of sample and sliding distance were 60 rpm, 6 mm/r and 8 m, respectively. Before testing, the surfaces of as-sprayed nHA coatings were polished using an abrasive paper of 1000 grit to minimize possible deviation caused by coating surface topography. Weights of the sample before and after wearing were measured using an electric balance with an

accuracy of 0.1 mg. The average weight loss from three tests for each spraying condition was used to evaluate the wear resistance of the coatings.

In Vitro Tests

In vitro tests were carried out by exposing 1 cm² surfaces of nHA coatings to Hank’s SBF. The specimens were held at a temperature of 37 ± 1 °C for 60 days. After the in vitro tests, the nHA coatings were rinsed using distilled water and then dried in air. Surface morphologies of the coatings after in vitro tests were inspected using SEM.

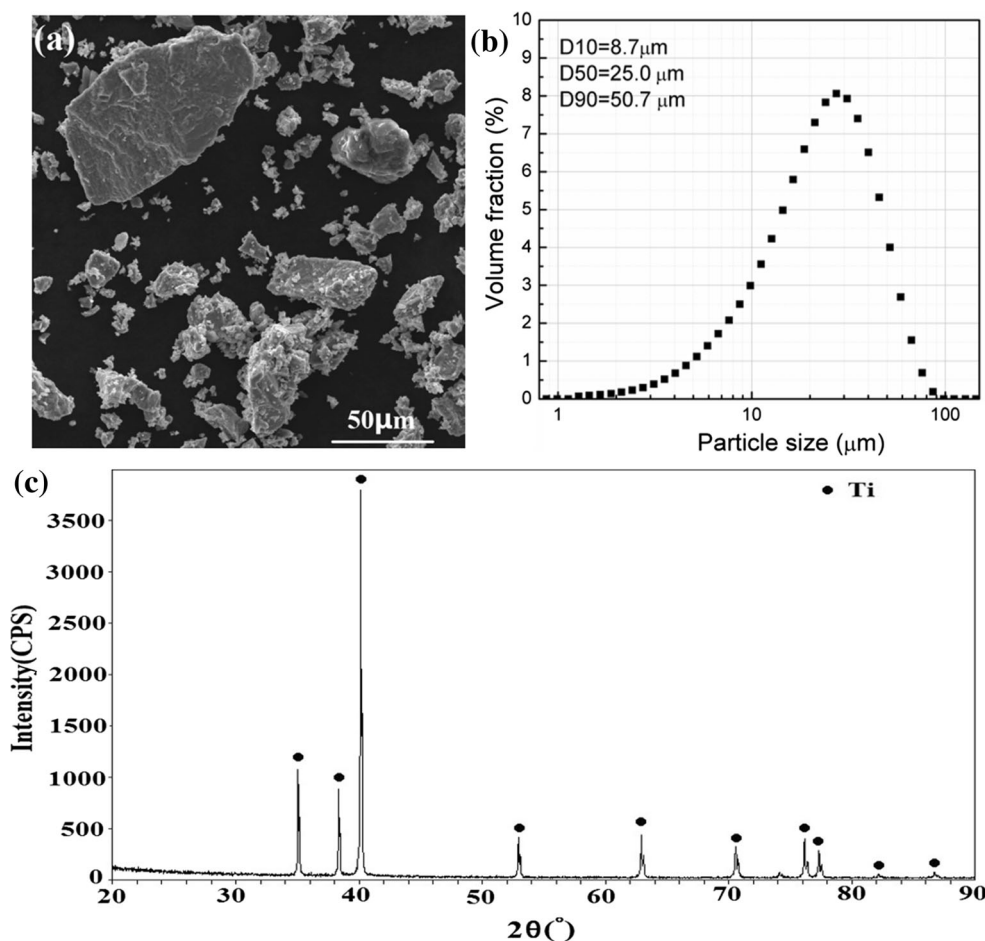
Results and Discussion

Characteristics of the Feedstock

Figure 2 shows the morphology, particle size distribution and XRD patterns of pure Ti feedstock. The Ti particles showed an angular morphology (Fig. 2a) with size ranging from 5 to 60 μm (Fig. 2b). The XRD pattern in Fig. 2(c) indicated that the Ti feedstock had a hexagonal

close-packed (HCP) lattice structure and not any other phase was detected. Figure 3 displays the morphology, particle size distribution, XRD pattern and TEM micrographs of the nHA feedstock. The starting nHA particles presented an irregular morphology (Fig. 3a) were agglomerated to larger sizes with a size distribution from 0.4 to 70 μm (Fig. 3b). It is noteworthy that the micro-size agglomerated particles improved the flow ability of the feedback powders which contributed to a stable powder feed rate during the coating spray. The XRD pattern shown in Fig. 3(c) indicated that no obvious impurity phase existed in as-received nHA powders. TEM graphs (Fig. 3d, e, and f) further confirmed the nanostructure and complete crystallization of the starting nHA powders. The particles in starting HA powders showed a needle-like morphology with a length of ~ 100 nm and a diameter of ~ 20 nm (Fig. 3d). Clear diffraction rings were identified, while halo characteristic was not noticeable from the selected area diffraction pattern, giving further evidence for full crystallization of nHA powders. From high-resolution TEM graphs of an individual nHA particle (Fig. 3f), clear lattice fringes were identified, corroborating the observed high crystallinity of the starting powders.

Fig. 2 Surface morphology (a), size distribution diagram (b) and XRD patterns (c) of Ti feedstock



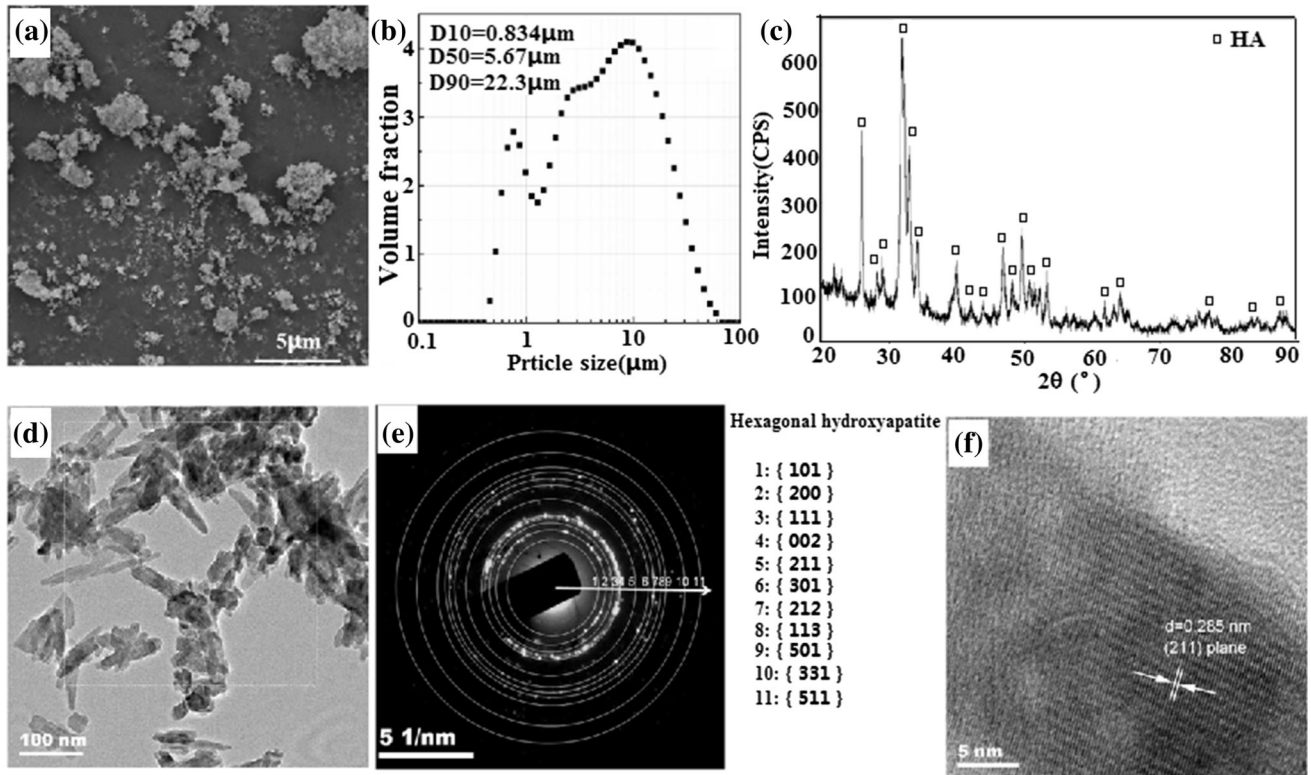


Fig. 3 Surface morphology (a), size distribution diagram (b), XRD patterns (c) and TEM results (d-f) of nHA feedstock; (d) is a bright field TEM micrograph and (e) is selected area diffraction pattern of

nHA powders; (f) is a high-resolution TEM micrograph of an individual nHA particle

Deformation Behavior of a Single Particle During Deposition

To achieve a better understanding of the formation mechanisms of Ti buffer layer and nHA coatings, deformation behavior of cold sprayed Ti and nHA splats impacting on stainless and Ti6Al4V substrates were examined. Figure 4 shows the morphologies of Ti and nHA splats attached on TC4 and SS substrates, respectively. Thin band or jet feature was observed at the rim of Ti splats (indicated by white arrows in Fig. 4a and b), which suggests localized plastic deformation of Ti splats. These characteristics were consistent with the modeling results of cold deposited irregular Ti particles on stainless steel substrates at the inlet temperature of 600 °C (Ref 22). However, significant plastic deformation of the Ti6Al4V and SS substrates was not detected. The deformations of the splats and substrates were influenced by their hardness in addition to other factors such as density, yield strength of particle material, particle size, velocity and temperature (Ref 29). In the present work, the microhardness of Ti particles measured on its cross section was 126.7 ± 22.7 HV_{0.01}, which is much lower than the surface microhardness of SS (251 ± 21.3 HV_{0.3}) or Ti6Al4V (263.3 ± 13.1 HV_{0.3}) substrate. The distinct hardness mismatch between the

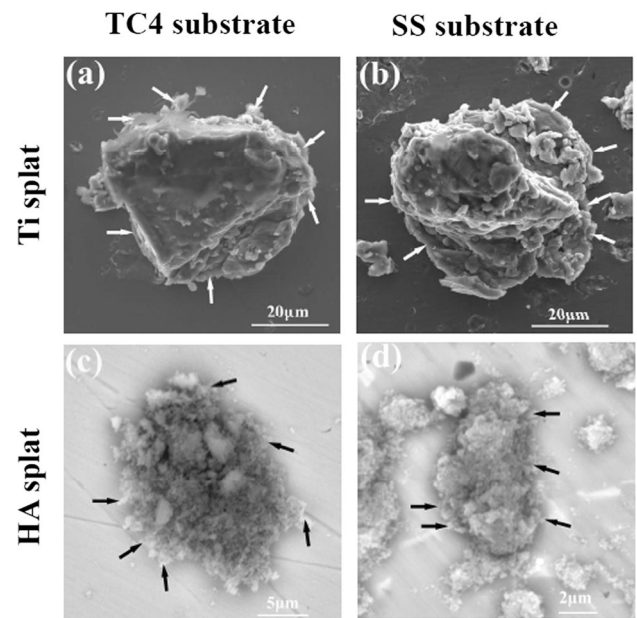


Fig. 4 Single splats morphologies impacting on different substrate: (a) Ti on TC4, (b) Ti on SS, (c) HA on TC4 and (d) HA on SS

particles and the substrates makes the plastic deformation mainly concentrate on the soft side (Ti particle) (Ref 26, 29). Figure 4(c) and (d) shows the morphologies of

nHA splats on SS and Ti6Al4V substrates, respectively. The cold deposited nHA splats exhibited an irregular hump-like shape with a rough surface, which was similar to that of cold deposited HA splats on Ti6Al4V substrate using spherical HA particles (Ref 27), but quite different from that of HA splats deposited by PS (Ref 18), MIPA (Ref 14), or suspension spraying (Ref 15). The rough surfaces of splats likely indicated that melting of particles did not occur during cold spray. Meanwhile, small stripes (indicated by arrows in Fig. 4) were observed on periphery of bonded nHA splats, whereas ripples or ripples were absent on substrate surface. This indicates that nHA splats underwent very limited deformation upon impacting on SS and Ti6Al4V substrates in the form of tiny nHA cluster movement, similar to that of WC-Co splats on WC-Co substrate (Ref 26). Cinca et al. (Ref 27) found that, under a shock compressive loading, plastic deformation of porous HA particles upon impacting underwent pore collapse, fragmentation and densification as well as grain refinement. As HA has poor intrinsic plasticity, it is possible that the main deformation mechanism during the coating deposition was pore collapse induced by coordinating deformation between the nanosized particles. EDS results manifested that the atom ratios of Ca to P of original powders and deposited splats were, respectively, 1.56 ± 0.13 and 1.55 ± 0.15 suggesting that significant decomposition of nHA did not occur during cold spray.

Microstructure of the Deposited nHA and Ti Coating

In previous experiments, nHA coating is deposited directly on TC4 alloy substrate (as shown in Fig. 5). It can be found that there is a crack (indicated by black arrows) between nHA coating and TC4 alloy substrate, it is further revealed that depositing directly nHA coating on TC4 substrate would lead to weak bonding between coating and substrate. Figure 6 and 7 show typical surface morphologies and cross-sectional microstructures of cold sprayed nHA and Ti coatings, respectively. It is clearly seen that Ti coating exhibited a porous structure (as shown in Fig. 6a) which is similar to that of Ti coating as reported in (Ref 24). The as-deposited nHA coatings exhibited a relatively smooth surface with some ditches (indicated by hollow black arrows in Fig. 6c) and pores (indicated by hollow white arrows in Fig. 6c). These ditches were formed by uneven and rather limited deformation of nHA particles and the pores were resulted from the low densification degree of nHA particles, which were in association with the low plasticity and kinetic energy of the sprayed particles (Ref 21, 27, 29). Moreover, some debris was also observed on nHA coating surface (indicated by black arrows in Fig. 6d) which was mostly crushed nHA particles. In addition, it

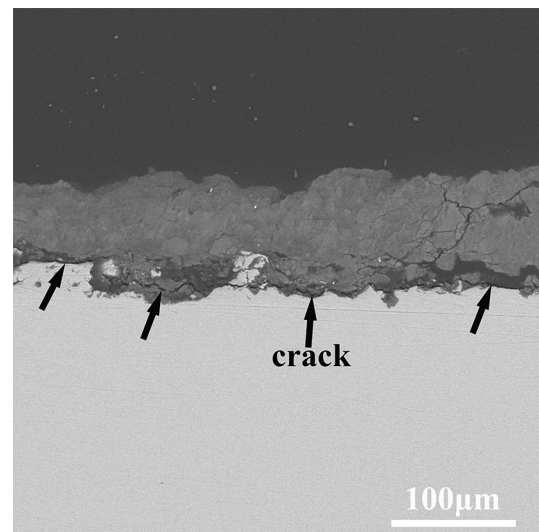


Fig. 5 Cross-sectional microstructure of nHA coating deposited on TC4 alloy substrate

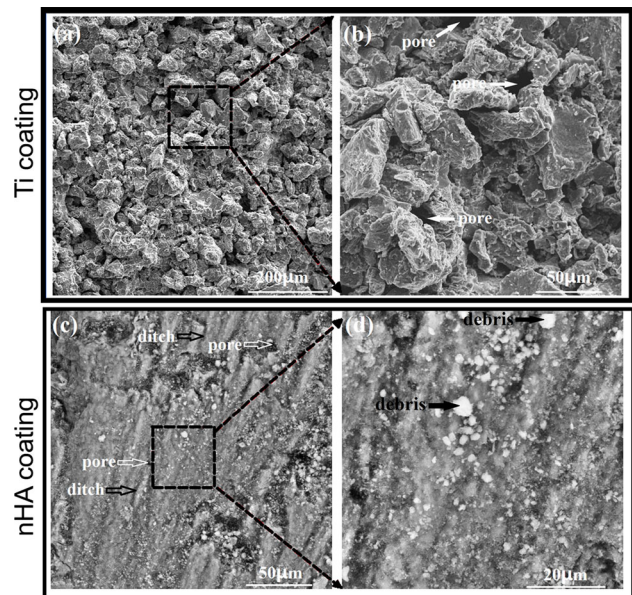


Fig. 6 Surface morphologies of the Ti butter layer coating (a, b) and nHA coating (c, d)

was noticed that nHA coating presented a homogeneous structure without visible lamella structures (as shown in Fig. 7). The interfaces of Ti coating/Ti6Al4V substrate and nHA coating/Ti coating exhibited a dense structure except for some pores on the interface of Ti coating/Ti6Al4V substrate. In contrast, an increment of coating porosity from the interface toward the coating surface was noticed in the cross section of cold sprayed Ti coating, similar to the observations in previous works (Ref 24). That is, a Ti buffer coating with a porous surface and a dense bottom layer was obtained. It is believed that such structure could

Fig. 7 (a) Cross-sectional microstructure and EDS of nHA/Ti bilayer coating and (b) closer view of nHA coating showing with a high magnification the area indicated by the square in (a)

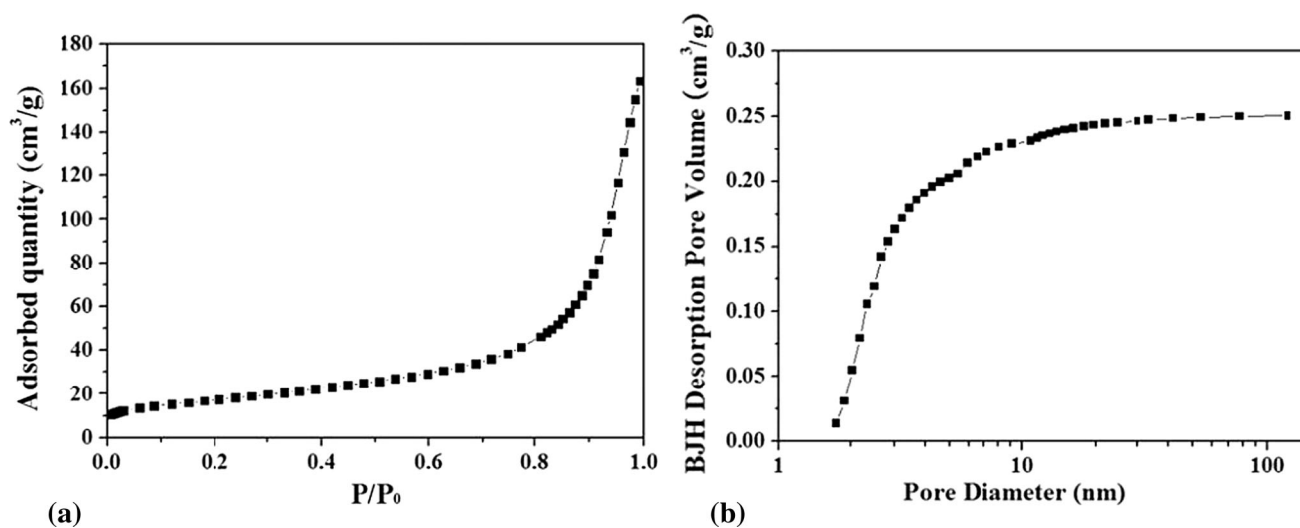
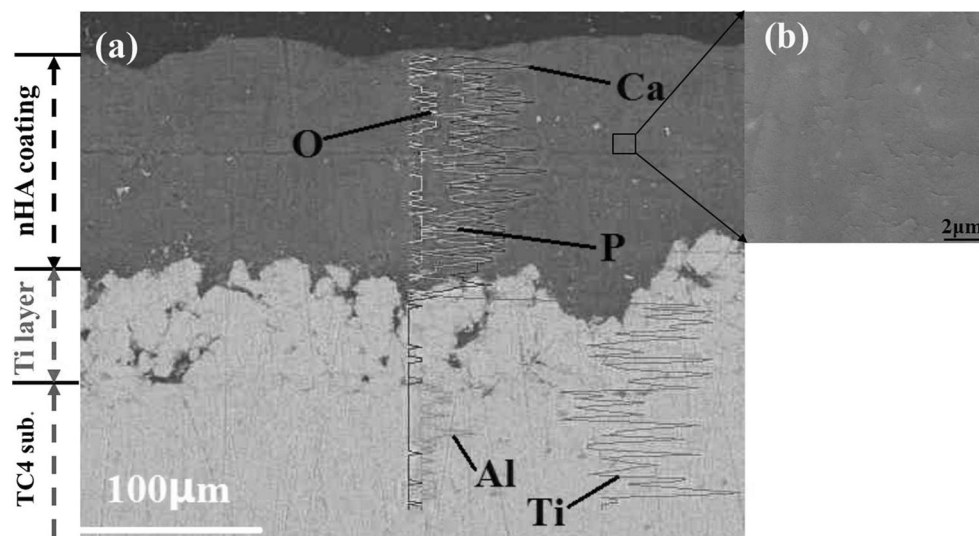


Fig. 8 (a) Nitrogen adsorption–desorption isotherms and (b) pore size distribution curves of nHA coating

benefit the adhesion of both the Ti/TC4 and HA/Ti interfaces. The dense bottom layer ensured the satisfactory bonding between Ti and TC4 substrate, while the porous top layer led to a high surface roughness of the Ti coating allowing penetration of HA particles.

In order to further analyze the porosity of nHA coating, nitrogen adsorption–desorption method was used. Figure 8 shows the results of nitrogen adsorption–desorption isotherm (as shown in Fig. 8a) and pore size distribution of nHA coating (as shown in Fig. 8b). The values of pore volumes estimated by BJH from desorption branch method are in the range 0.014–0.25 cm³ g^{−1} for the nHA coating, and the average pore diameter was about 13–16 nm.

In order to investigate possible modification of chemical compositions during the coating formation, EDS analyses

of the coatings were conducted on coatings cross section. The atom ratio of Ca to P in deposited coating was 1.54 ± 0.07 , which was nearly identical to that of the original nHA powder. This fact confirmed that no significant decomposition of nHA occurred during coating formation by using cold spraying process.

Figure 9 shows the TEM micrographs of as-sprayed nHA coatings. The needle-like morphologies of nHA particles retained after coating deposition (Fig. 3d). However, the length of the HA particles after deposition was smaller than that in original powder. It is likely that needle-like HA particles were broken due to the high-velocity impact during cold spray. Similar phenomenon was observed in cold spray deposition of sintered HA particles with a spherical shape (Ref 27) and cold spray of agglomerated

Fig. 9 TEM observations of the cold sprayed HA coating. (a) low magnification BF-TEM image, (b) the selected area diffraction pattern, (c) the high magnification BF-TEM image showing the morphology of HA particles and (d) HR-TEM image of a randomly selected HA particle. The as-sprayed nHA coating was scraped with a knife blade and the scraped off particles are used as the TEM sample

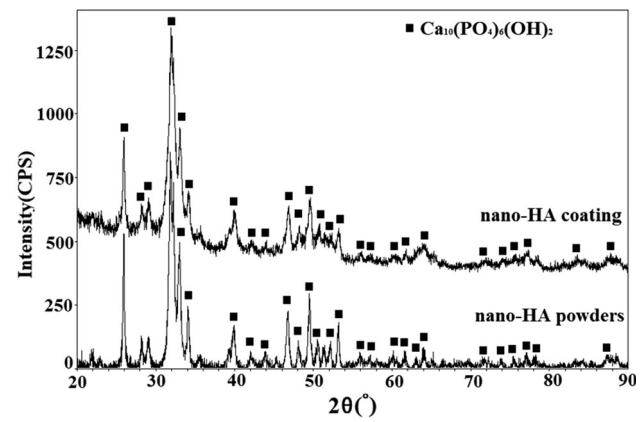
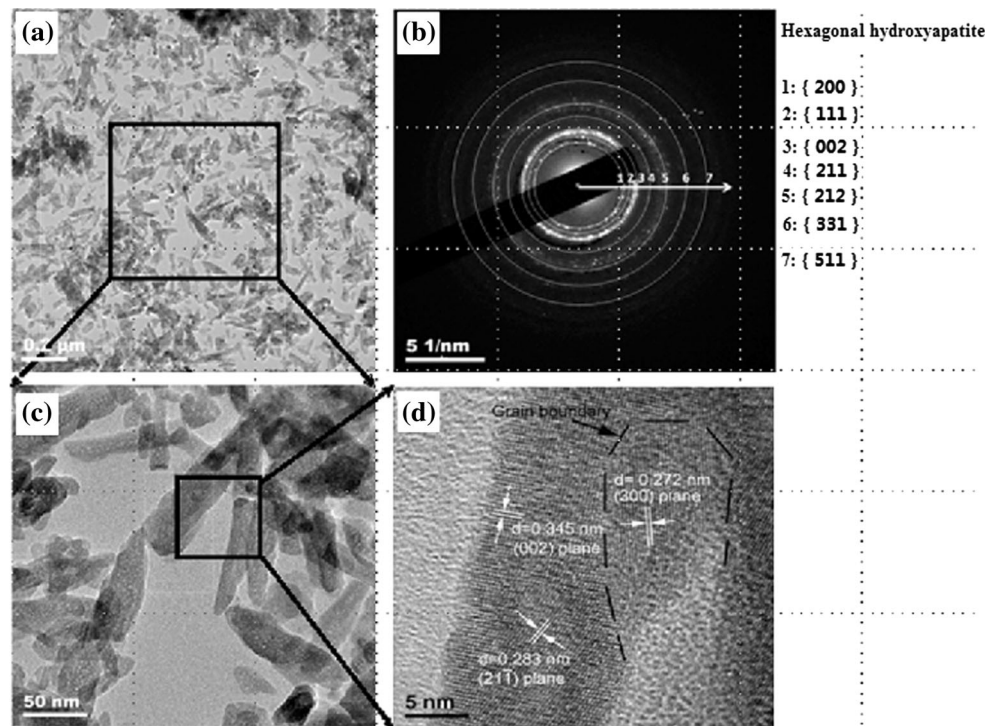


Fig. 10 XRD patterns of cold sprayed nHA coatings and nHA powders

WC-Co particles (Ref 26). Moreover, the diffraction pattern in Fig. 9(b) indicated that the crystallinity of the particles was not evidently affected by the coating deposition process. From Fig. 9(d), grain boundaries within individual splats were clearly observed, however, they were absent in the feedstock (Fig. 3f). It is hence inferred that grain refinement of the nHA particles occurred during spray, which requires further endeavors. Further efforts are required to make the grain refining mechanisms clear in future. Moreover, clear lattice fringes indicated that crystalline structure of the nHA was not altered during coating deposition (as marked with the white lines in Fig. 9d).

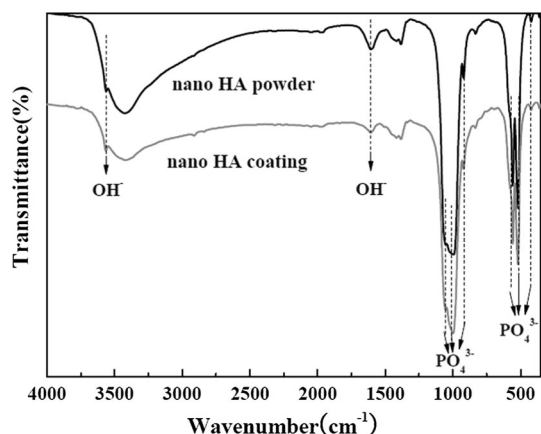
Phase Composition and Structure of nHA Coating

Figure 10 shows XRD patterns of the as-sprayed Ti and nHA coatings as well as the original powders. It was noticed that, by comparing with the feedstock, there was no new peak appeared in coatings. Neither TTCP, TCP and CaO phases nor ACP usually included in thermal sprayed HA coatings were not observed (Ref 17). Moreover, peaks in XRD patterns of nHA powders and as-sprayed coatings are identical with standard HA peaks (JCPDS 9-432). The crystallinity of as-sprayed nHA coatings evaluated by using Eq 1 was 100% giving further evidence that amorphization did not occur during coating deposition. In addition, the interplanar spacing (d_{hkl}) and full width at half maximum ($FWHM_{hkl}$) of original nHA powders and coatings were estimated from XRD data and are listed in Table 2. It was demonstrated that the d_{hkl} and $FWHM_{hkl}$ of nHA coatings were identical to those of the nHA feedstock. This indicated that the microstrain in HA lattice was negligible and corroborated the fact that sprayed HA particles underwent very limited plastic deformation upon high-speed impact.

FTIR analysis has been commonly employed to identify chemical bands and groups in materials. The characteristic peaks in FTIR spectrum of as-sprayed nHA coatings (as shown by curve of gray color in Fig. 11) were identical with those of original powders (as shown by curve of black color in Fig. 11). Moreover, the peaks in FTIR spectra of both original powders and as-deposited coatings were consistent with those of typical HA and other apatite

Table 2 d_{hkl} and $FWHM_{hkl}$ for original nHA powders and cold sprayed coatings derived from XRD data

Peaks, hkl		002	102	211	112	300	202	130	222	213
d_{hkl} , Å	Powder	3.42932	3.1617	2.80461	2.77324	2.71106	2.62822	2.25406	1.93937	1.83934
	Coating	3.42677	3.1619	2.79782	2.77094	2.70816	2.61943	2.25394	1.93935	1.83932
$FWHM_{hkl}$, rad.	Powder	0.241	0.192	0.478	0.594	0.372	0.297	0.423	0.402	0.271
	Coating	0.21	0.208	0.546	0.596	0.386	0.323	0.415	0.408	0.269

**Fig. 11** FTIR spectra of cold sprayed nHA coatings and original nHA powders

biomaterials as reported in references (Ref 5, 18). The sharp peaks at 603.69, 567.05 and 470.61 cm^{-1} in the spectra of both original powders and coatings, were attributable to the triply degenerate asymmetric O-P-O bending band [4: 603 cm^{-1} and 562 (Ref 2), 602 and 563 cm^{-1} (Ref 5)] and O-P-O bending band [2: 470 cm^{-1} (Ref 2), 471 cm^{-1} (Ref 5)]. The peaks at 962.1 cm^{-1} in the spectrum of the powders and 962.80 cm^{-1} in the spectrum of the coatings corresponded to characteristic peak of PO_4 group [960 cm^{-1} (Ref 16)]. The band at 1038.62 cm^{-1} and the weak peak at 1094.55 cm^{-1} in the spectrum of the original powders, and the peak at 1035.73 cm^{-1} and the weak peak at 1092.63 cm^{-1} in the spectrum of as-deposited coatings, corresponded to the asymmetric O-P-O stretching band [3: 1034 cm^{-1} (Ref 10), 1040 cm^{-1} (Ref 18), 1096 cm^{-1} (Ref 18), 1099 cm^{-1} (Ref 5)]. The peak at 3569–3596 cm^{-1} was attributed to the stretching modes of OH^{-1} in nHA coatings (Ref 18). The broad peaks at 3430 and 1640 cm^{-1} were attributed to OH^{-1} stretching vibration and adsorbed molecular of water (Ref 5). In addition, in these spectra, a weak absorption peak at 1418.58 cm^{-1} of the original powders and the peak at 1419.56 cm^{-1} of as-deposited coatings, and the common peaks at 875.64 cm^{-1} were characteristic peaks of carbonate (Ref 30). These carbonates observed in both nHA powders and deposited coatings may be attributed to incomplete

pyrolysis of precursors dissolved into the nHA crystal and/or atmosphere (Ref 31). From aforesaid experimental results, it was recognized that there were no additional phases such as ACP, TCP, TTCP and CaO within cold spray nHA coatings. The chemical compositions, phase constitutions and structures of original nHA powders were transmitted to as-deposited coatings by using cold spray process.

Mechanical and Biological Behaviors of nHA Coating

Mechanical properties of cold sprayed nHA coatings were characterized in terms of microhardness, adhesion strength and abrasive wear resistance. Experimental results showed that the microhardness, bond strength of as-deposited nHA coating were HV0.1: $26.46 \pm 1.95 \text{ kg/mm}^2$ and 2.2 MPa, respectively. The microhardness of cold sprayed nHA coatings was higher than that of cold sprayed HA coatings (Ref 27) and comparable to that of sintered HA in humid air (Ref 9), and lower than that of APS (Ref 18), HVOF (Ref 15), MIPS (Ref 14) sprayed ones. The bond strength of cold sprayed nHA coatings was comparable to that reported in (Ref 32) and lower than that of APS (Ref 18), HVOF (Ref 15), MIPS (Ref 14) sprayed HA and cold sprayed HA/Ti coatings using HA-Ti mixture powders (Ref 33). Figure 12 shows the surface morphology of failed adhesion test specimens. It is found that fracture mainly occurred at the nHA coating/Ti buffer layer interface and inner nHA coating. It is known that the bond strength depends on both cohesive and adhesive strengths of a coating (Ref 14). Plastic deformation of incident particles and/or substrate or pre-deposited splats is the basis of the splats/substrate interface bonding and intersplats bonding (Ref 22, 23). However, under the spraying conditions investigated, the nHA coatings were built up by deformation of particles at about only 300 °C, which was far below the melting point of HA. At such low temperature, the deformation and densification of nHA splats during the spray was mainly attributed to the pore collapse induced by relative displacement of the nano-HA particles. The inter-particle bonding of cold deposited nHA coatings was

Fig. 12 Photographs of failed adhesion test specimens

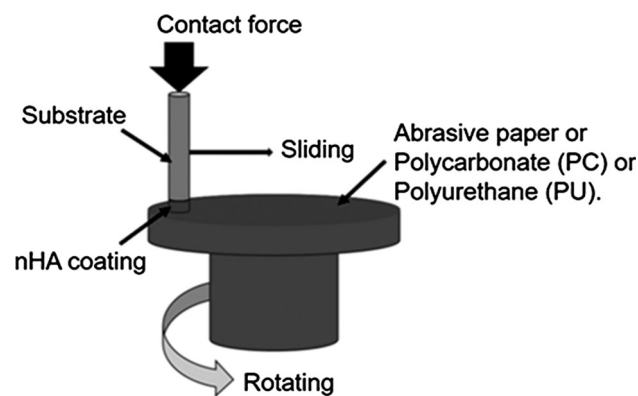
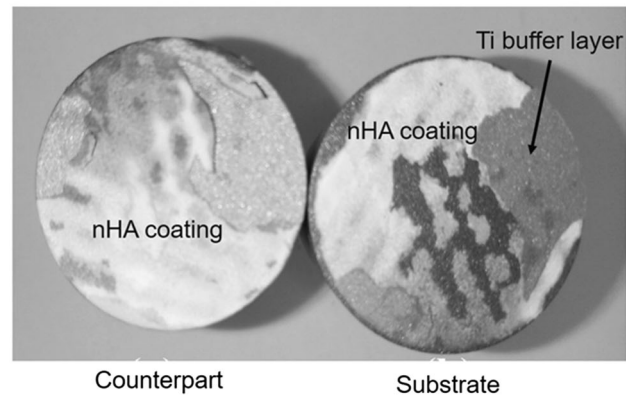
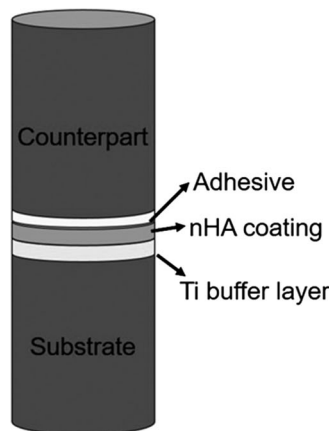


Fig. 13 Schematic diagram of pin-on-disk test

mainly dominated by Van de Waals force and mechanical interlocking, which further contributed to the lower hardness and bond strength of cold sprayed nHA coatings.

To evaluate the abrasive wear of the coatings, pin-on-disk wear tests (Fig. 13) were conducted. PC and PU sheets with mechanical properties comparable to artificial ligaments (Ref 34, 35) were used for wear counterparts. No obvious weight loss of coatings was detected after sliding against PC and PU for 8 m at 2 N.

Although above results demonstrated that cold sprayed nHA coatings exhibited relatively low hardness and bonding strength, strategies such as modifying powder microstructures, spraying at higher pressures and post-spray annealing can potentially improve the mechanical performance. Firstly, sintering the starting nHA feedstock at a suitable temperature can strengthen the interparticle bonding and thus improve the hardness and adhesion of the resultant coating. Secondly, higher spraying pressures can lead to higher particle impact velocity and thus stronger peening which benefits for denser coating and stronger mechanical interlocking between the coating and the substrate. In addition, post-spray annealing at a suitable temperature is capable to strengthen the intersplat bonding while maintaining nanostructures of the nHA coatings.

Surface Morphology of nHA Coating After Immersed in SBF

Figure 14 shows the surface morphologies of cold sprayed nHA coatings after soaking in Hank’s SBF for 60 days. It was found that the surface morphologies of soaked coatings were quite different to those of as-deposited one. The nHA debris on the surface of as-deposited coatings (as shown in Fig. 6d) completely disappeared and numerous spherical particles were embossed on the smooth surface. This indicated that dissolving and precipitation occurred during soaking in SBF (Ref 34). EDS analyses implied that the atom ratio of Ca to P of those precipitations was 1.59 ± 0.21 , which was comparable to that of the apatite phase. The apatite-forming ability of the samples soaked in SBF was considered as an indication of the osseointegration capability (Ref 34, 35). Therefore, these prominent precipitations of apatite formed in soaking demonstrated great abilities in the apatite forming of cold deposited nHA coatings after soaking in SBF solution.

Conclusions

In the present work, nHA coatings were successfully deposited on SS and TC4 substrates via using cold spraying technique. A Ti butter layer was primarily cold sprayed on the substrate, which was crucial for coating deposition. Our results demonstrated that dense nHA coatings were achievable by using cold spray technique while inhibiting dehydration, decomposition and phase alteration of the feedstock powders, as encountered when preparing HA coatings using conventional deposition techniques. Cold spraying was identified as a promising technique for preparing nanostructured nHA coatings. Comprehensive investigations of structures of both individual splats and deposited coatings revealed that due to the low processing temperature, intersplat bonding mainly derived from

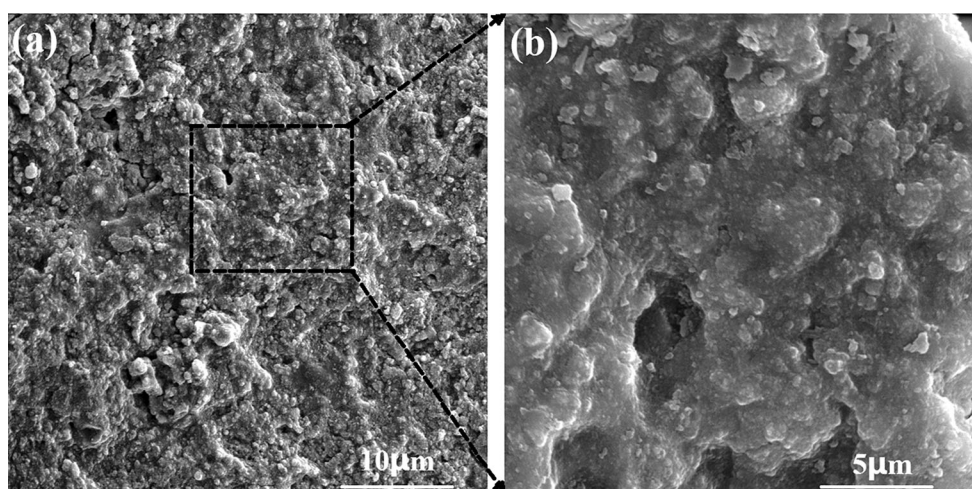


Fig. 14 Surface morphologies of cold sprayed nHA coatings after soaking in SBF solutions for 60 days

mechanical interlocking and Van der Waals force. As-deposited coatings exhibited lower hardness and bonding strength as compared with plasma sprayed HA coatings. Nevertheless, cold sprayed nHA coatings exhibited a high wear resistance when sliding against PU and PC. As-deposited HA coatings showed good apatite formation ability during soaking in SBF, owing to coating nanostructures.

Acknowledgments This work was financially supported by National Science Foundation of China (Grant Number 51461022, 51861012), the Science Technology Project of Jiangxi Province (Grant Number 20171BAB206007), Science and Technology Project of Jiangxi Educational Bureau (Grant Number GJJ171062), and Base and Talent/Outstanding Young Talent Program of Jiujiang Science and Technology (Grant Number [2016]43 No.75).

References

1. M. Hasniyati, H. Zuhailawati, R. Sivakumar, B.K. Dhindaw, and S.N.F.M. Noor, Cold Spray Deposition of Hydroxyapatite Powder Onto Magnesium Substrates for Biomaterial Applications, *Surf. Eng.*, 2015, **31**(11), p 867-874
2. H.H. Dai, P. Wang, P. Liu, X.K. Liu, F.C. Ma, and J. Zhao, HA Coating Fabricated by Electrochemical Deposition on Modified Ti6Al4V Alloy, *Surf. Coat. Technol.*, 2015, **277**, p 203-209
3. D.X. Liu, K. Savino, and M.Z. Yates, Coating of Hydroxyapatite Films on Metal Substrates by Seeded Hydrothermal Deposition, *Surf. Coat. Technol.*, 2011, **205**(16), p 3975-3986
4. A.T. Rad, M. Solati-Hashjin, N.A.A. Osman, and S. Faghihi, Improved Bio-physical Performance of Hydroxyapatite Coatings Obtained by Electrophoretic Deposition at Dynamic Voltage, *Ceram. Int.*, 2014, **40**(8), p 12681-12691
5. D.T. Thanh, P.T. Nam, N.T. Phuong, L.X. Que, N.V. Anh, T. Hoang, and T.D. Lam, Controlling the Electrodeposition, Morphology and Structure of Hydroxyapatite coating on 316L Stainless Steel, *Mater. Sci. Eng.*, 2013, **33**(4), p 2037-2045
6. U. Anjaneyulu, D.K. Pattanayak, and U. Vijayalakshmi, Snail Shell Derived Natural Hydroxyapatite: Effects on NIH-3T3 Cells for Orthopedic Applications, *Adv. Manuf. Proc.*, 2016, **31**(2), p 206-216
7. W.S. Jing, M.H. Zhang, L. Jin, J. Zhao, Q. Gao, M. Ren, and Q.Y. Fan, Assessment of Osteoinduction Using a Porous Hydroxyapatite Coating Prepared by Micro-arc Oxidation on a New Titanium Alloy, *Int. J. Surg.*, 2015, **24**(Pt A), p 51-56
8. J.A. Toque, M.K. Herliansyah, M. Hamdi, A. Ide-Ekessabi, and I. Sopyan, Adhesion Failure Behavior of Sputtered Calcium Phosphate Thin Film Coatings Evaluated Using Micro-scratch Testing, *J. Mech. Behav. Biomed. Mater.*, 2010, **3**(4), p 324-330
9. T.M. Sridhar, U. KamachiMudali, and M. Subbaiyan, Sintering Atmosphere and Temperature Effects on Hydroxyapatite Coated Type 316L Stainless Steel, *Corros. Sci.*, 2003, **45**(10), p 2337-2359
10. H. Farnoush, A. Sadeghi, A.A. Bastami, F. Moztafzadeh, and J.A. Mohandesi, An Innovative Fabrication of Nano-HA Coatings on Ti-CaP Nanocomposite Layer Using a Combination of Friction Stir Processing and Electrophoretic Deposition, *Ceram. Int.*, 2013, **39**(2), p 1477-1483
11. M.F. Mohd Yusoff, M.R. AbdulKadir, N. Iqbal, M.A. Hassan, and R. Hussain, Dipcoating of Poly(ϵ -caprolactone)/Hydroxyapatite Composite Coating on Ti6Al4V for Enhanced Corrosion Protection, *Surf. Coat. Technol.*, 2014, **245**(1), p 102-107
12. C.F. Koch, S. Johnson, D. Kumar, M. Jelinek, D.B. Chrisey, A. Doraiswamy, C. Jin, R.J. Narayan, and I.N. Mihailescu, Pulsed Laser Deposition of Hydroxyapatite Thin Films, *Mater. Sci. Eng. C*, 2007, **27**(3), p 484-494
13. R. Palanivelu, S. Kalainathan, and A. Ruban Kumar, Characterization Studies on Plasma Sprayed (AT/HA) Bi-layered Nano Ceramics Coating on biomedical Commercially Pure Titanium Dental Implant, *Ceram. Int.*, 2014, **40**(6), p 7745-7751
14. X.M. Liu, D.Y. He, Y.M. Wang, Z. Zhou, G.H. Wang, Z. Tan, and Z.J. Wang, The Influence of Spray Parameters on the Characteristics of Hydroxyapatite In-Flight Particles, Splats and Coatings by Micro-plasma Spraying, *J. Therm. Spray Technol.*, 2018, **27**(4), p 667-679
15. R.B. Heimann, Plasma-Sprayed Hydroxylapatite Coatings as Biocompatible Intermediaries Between Inorganic Implant Surfaces and Living Tissue, *J. Therm. Spray Technol.*, 2018, **27**, p 1-26
16. G. Bolelli, D. Bellucci, V. Cannillo, R. Gadow, A. Killinger, L. Lusvardi, P. Müller, and A. Sola, Comparison Between Suspension Plasma Sprayed and High Velocity Suspension Flame Sprayed Bioactive Coatings, *Surf. Coat. Technol.*, 2015, **280**, p 232-249

17. Y.S. Tian, X.L. Qian, and M.Q. Chen, Effect of Saturated Steam Treatment on the Crystallinity of Plasma-Sprayed Hydroxyapatite Coatings, *Surf. Coat. Technol.*, 2015, **266**, p 38-41
18. L. Sun, C.C. Berndt, and C.P. Grey, Phase, Structural and Microstructural Investigations of Plasma Sprayed Hydroxyapatite Coatings, *Mater. Sci. Eng. A*, 2003, **360**(1-2), p 70-84
19. R.C. Dykhuizen and M.F. Smith, Gas Dynamic Principles of Cold Spray, *J. Therm. Spray Technol.*, 1998, **7**(2), p 205-212
20. D. Cruz, M.Á. Garrido, Á. Rico, C.J. Múñez, and P. Poza, Wear Resistance of Cold Sprayed Al Alloys for Aeronautical Repairs, *Surf. Eng.*, 2018, **34**, p 1-9
21. C.Y. Chen, X.L. Xie, Y.C. Xie, X.C. Yan, C.J. Huang, S.H. Deng, Z.M. Ren, and H.L. Liao, Metallization of Polyether Ether Ketone (PEEK) by Copper Coating Via Cold Spray, *Surf. Coat. Technol.*, 2018, **342**, p 209-219
22. K. Yang, W.Y. Li, X.W. Yang, and Y.X. Xu, Anisotropic Response of Cold Sprayed Copper Deposits, *Surf. Coat. Technol.*, 2018, **335**, p 219-227
23. B. Song, K.T. Voisey, and T. Hussain, High Temperature Chlorine-Induced Corrosion of Ni50Cr Coating: HVOLF, HVOGF, Cold Spray and Laser Cladding, *Surf. Coat. Technol.*, 2018, **337**, p 357-369
24. V. Champagne and D. Helfritch, The Unique Abilities of Cold Spray Deposition, *Int. Mater. Rev.*, 2016, **61**(7), p 1-19
25. A.M. Vilardell, N. Cinca, A. Concustell, S. Dosta, I.G. Cano, and J.M. Guilemany, Cold Spray as an Emerging Technology for Biocompatible and Antibacterial Coatings: State of Art, *J. Mater. Sci.*, 2015, **50**(13), p 4441-4462
26. X. Chen, H.T. Wang, G.C. Ji, X.B. Bai, and Z.X. Dong, Deposition Behavior of Nanostructured WC-23Co Particles in Cold Spraying Process, *Adv. Manuf. Eng.*, 2015, **31**(11), p 1507-1513
27. N. Cinca, A.M. Vilardell, S. Dosta, A. Concustell, I. Garcia Cano, J. Maria Guilemany, S. Estradé, A. Ruiz-Caridad, and F. Peiró, A New Alternative for Obtaining Nanocrystalline Bioactive Coatings: Study of Hydroxyapatite Deposition Mechanisms by Cold Gas Spraying, *J. Am. Ceram. Soc.*, 2016, **99**(4), p 1420-1428
28. S. Yin, P.J. He, H.L. Liao, and X.F. Wang, Deposition Features of Ti Coating Using Irregular Powders in Cold Spray, *J. Therm. Spray Technol.*, 2014, **23**(6), p 984-990
29. M.R. Rokni, S.R. Nutt, C.A. Widener, V.K. Champagne, and R.H. Hrabec, Review of Relationship Between Particle Deformation, Coating Microstructure, and Properties in High-Pressure Cold Spray, *J. Therm. Spray Technol.*, 2017, **26**(6), p 1308-1355
30. C.L. Chu, T. Hu, L.H. Yin, Y.P. Pu, Y.S. Dong, P.H. Lin, C.Y. Chung, K.W.K. Yeung, and P.K. Chu, Microstructural Characteristics and Biocompatibility of a Type-B Carbonated Hydroxyapatite Coating Deposited on NiTi Shape Memory Alloy, *Biomed. Mater. Eng.*, 2009, **19**(6), p 401-408
31. R.N. Panda, M.F. Hsieh, R.J. Chung, and T.S. Chin, FTIR, XRD, SEM and Solid State NMR Investigations of Carbonate-Containing Hydroxyapatite Nano-particles Synthesized by Hydroxide-Gel Technique, *J. Phys. Chem. Solids*, 2003, **64**(2), p 193-199
32. Y.C. Yang and E. Chang, Influence of Residual Stress on Bonding Strength and Fracture of Plasma-Sprayed Hydroxyapatite Coatings on Ti-6Al-4V Substrate, *Biomaterials*, 2001, **22**(13), p 1827-1836
33. A. Choudhuri, P.S. Mohanty, and J. Karthikeyan, Bio-ceramic composite coatings by cold spray technology. in *Proceedings of the International Thermal Spray Conference*, ed. by B.R. Marple, M.M. Hyland, Y.-C. Lau, C.-J. Li, R.S. Lima, and G. Montavon, 4-7 May 2009 (Las Vegas, Nevada, USA, 2009), ASM International, p 391-396
34. G. Bolelli, D. Bellucci, V. Cannillo, L. Lusvardi, A. Sola, N. Stiegler, P. Müller, A. Killinger, R. Gadow, L. Altomare, and L.D. Nardo, Suspension Thermal Spraying of Hydroxyapatite: Microstructure and In Vitro Behavior, *Mater. Sci. Eng. C*, 2014, **34**(34C), p 287-303
35. H. Tang, D.Z. Yu, Y. Luo, and F.P. Wang, Preparation and Characterization of HA Microflowers Coating on AZ31 Magnesium Alloy by Micro-arc Oxidation and a Solution Treatment, *Appl. Surf. Sci.*, 2013, **264**(1), p 816-822